Journal of Applied Physics

Insights into nonvolatile resistive switching in monolayer hexagonal boron nitride

Cite as: J. Appl. Phys. **132**, 224302 (2022); https://doi.org/10.1063/5.0128682
Submitted: 29 September 2022 • Accepted: 12 November 2022 • Published Online: 08 December 2022

Sanchali Mitra and Santanu Mahapatra

AIP Publishing

Journal of Applied Physics ARTICLE scitation.org/journal/jap

Insights into nonvolatile resistive switching in monolayer hexagonal boron nitride

Cite as: J. Appl. Phys. **132**, 224302 (2022); doi: 10.1063/5.0128682
Submitted: 29 September 2022 · Accepted: 12 November 2022 ·
Published Online: 8 December 2022

Sanchali Mitra and Santanu Mahapatra[a)]

AFFILIATIONS

Nano-Scale Device Research Laboratory, Department of Electronic Systems Engineering, Indian Institute of Science (IISc) Bangalore, Bangalore - 560012, India

[a)]**Author to whom correspondence should be addressed:** santanu@iisc.ac.in

ABSTRACT

A recent demonstration of nonvolatile resistive switching in monolayer hexagonal boron nitride (h-BN) has paved the way for the development of the thinnest memory devices feasible. Nevertheless, the exact mechanism of such remarkable resistive switching has remained obscure, which may hinder the optimization of such attractive technology. Here, we present the first dynamic description of the resistive switching process in a Ni/monolayer h-BN/Ni device at an atomistic level by employing reactive molecular dynamics simulations. We show that with the application of a suitable bias, the h-BN layer moves vertically and peels off Ni ions from the electrode, which gets adsorbed in the N vacancy center. From density-functional-theory based electron-localization-function calculations, we confirm that N vacancy generates highly delocalized electrons around the vacancy location resulting in the adsorption of Ni ions, though such a phenomenon is not likely in case of B vacancy due to the absence of electronic states around the defect center. We demonstrate the restoration of Ni ions with the application of reverse bias in case of bipolar switching, and by rising temperature in case of unipolar switching, which agrees with the experimental observations. Finally, we conduct *ab initio* quantum transport calculation to find an increase in zero-bias conductivity of about 7.4 times after the Ni ion adsorption. This atomistic insight enables precise defect-engineering in 2D materials for the realization of h-BN based high-performance memristive crossbar array.

I. INTRODUCTION

Resistive switching (RS) devices have aroused widespread attention as the new paradigm in next-generation nonvolatile storage and ultrahigh-speed computing.[1–4] After the theoretical discovery of the existence of a memristor in 1971,[5] the first device using Pt/TiO_2/Pt-based metal/insulator/metal (MIM) structure was produced in 2008.[6] Subsequently, remarkable progress has been made in the mechanism and performance of the memristor. Primarily, these devices are fabricated by stacking insulating transition-metal oxides vertically between two metal electrodes.[7–9] The RS mechanisms of these devices are attributed to the migration of metal ions[10–12] or oxygen vacancies.[13,14] However, oxide being a 3D bulk material, these devices operate at high voltage with a high switching time. Replacing bulk oxide with atomically thin 2D materials can significantly upgrade the device's performance in ultrathin, super-integrated, low-power, and high-speed electronic circuits.[15–17] A surge of experiments is carried out to develop memristors using 2D materials for their possible applications in neuromorphic computing,[18,19] data encryption,[20] RF switches,[21,22] and photoelectronic devices.[23,24]

Owing to the wide bandgap and fascinating properties,[25–27] hexagonal boron nitride (h-BN) is gaining interest in RS devices. In 2017, Lanza and coworkers reported RS in multilayer h-BN stacked vertically between different electrodes.[28] These devices possess the co-existence of bipolar nonvolatile and volatile switching with low voltages around 0.4 V, high ON–OFF current ratio, and long retention time. Furthermore, using h-BN, high-performance electronic synapses were fabricated with both short-term and long-term plasticity.[29] Zhuang *et al.* reported nonvolatile nonpolar RS in multilayer h-BN based devices having Ti/h-BN/Au structure.[30] Multilayer h-BN is further used as RS material in high-density memristive crossbar array to model an artificial neural network for image recognition.[31–33] In addition to pure h-BN, h-BN/ graphene heterostructures are also used as RS layers in memristive devices.[33–35] The thinnest memristive device has been fabricated using monolayer (ML) h-BN featuring unipolar and bipolar

switching with formation of free characteristics, high on/off ratio (up to 10^7), and fast switching speed (<15 ns).[36] These atomically thin devices are used to create analog switches for applications in radio, 5G, and terahertz communication systems.[22] The switches exhibit high-frequency cutoff (>120 THz), low insertion loss, high power handling, and nanosecond switching speed. Despite the magnificent progress in the development of h-BN based memristive devices, we have a limited understanding of the origin of RS in it. Metal ion adsorption in B and N vacancy has been proposed as a possible mechanism of switching.[36] However, no dynamic observation of the ion adsorption is reported; therefore, several key issues remain unclear. Microscopy and ground state quantum-mechanical calculations deficit the spatial and temporal resolution required to describe the switching phenomena. Real-time simulations with external bias are essential to investigate the complete switching cycle. In earlier works, the RS process in bulk oxide[12] and ML MoS_2[37] has been described using molecular dynamics (MD) simulations. However, to our best knowledge, no real-time exploration of the bipolar and unipolar switching mechanisms in h-BN has been reported till date.

This work presents the first dynamic description of the RS process in ML h-BN at an atomistic level by employing reactive MD simulations. Au and Ni electrodes were used in the experiments to fabricate the thinnest memory device.[36] Ni electrode is chosen in this simulation due to the availability of applicable interatomic potential between h-BN and Ni atoms. We found that N vacancies are primarily responsible for RS in h-BN. The formation of conducting nano filament involves peeling off Ni ions from the electrode and adsorbing them in the vacancy centers at a critical applied bias. Quantum transport calculations clearly identify two distinct resistance states before and after Ni adsorption. A rise of zero-bias conductivity of about 7.4 times is measured while switching from the high resistance state (HRS) to the low resistance state (LRS).

II. COMPUTATIONAL DETAILS

MD simulations are performed using the LAMMPS package.[38] KOKKOS[39] package of LAMMPS is used to enable GPU acceleration. For visualization, VESTA[40] and OVITO[41] are used. Reactive force field (ReaxFF) parameters for B–N and Ni–Ni pairs are obtained from Refs. 42 and 43, respectively, while the B–Ni and N–Ni pair potentials are taken from Ref. 44. The time integration of Newton equations is performed using the velocity Verlet algorithm with a time step of 0.5 fs. Simulations are performed in an isothermal-isobaric environment with a Nose/Hoover temperature thermostat and a Nose/Hoover pressure barostat (NPT ensemble). Periodic boundary conditions are applied in all three directions. A sufficiently thick vacuum region (>30 Å) is inserted in the out of plane (z) direction to avoid any spurius interaction between periodic replicas. To build the device, first, the Ni/h-BN interface is formed by QuantumATK interface builder module.[45] To build the interface, unit cells of Ni ⟨111⟩ surface and h-BN are rotated 180° with respect to each other and matched by applying mean strain 0.31% in the h-BN layer. Interlayer distance is evaluated from geometry optimization using DFT calculations. After creating the interface, the Ni atoms are mirrored on the other side of h-BN to create a Ni/h-BN/Ni structure. To update the charge distributions in every step of the MD simulation, ReaxFF is coupled with a charge equilibration (QEq) method.[46] In QEq, the atomic charges are updated by minimizing the electrostatic energy of the system with the constraint of constant total charge. The total energy in a molecule or periodic system is expressed as $E(Q_1, Q_2, Q_3, \ldots, Q_N) = \sum_{A=1}^{N} \left(E_A + \chi_A^0 Q_A + \frac{1}{2} J_{AA}^0 Q_A^2 + \sum_{B>A}^{N} J_{AB} Q_A Q_B\right)$, where χ_A^0 and J_{AA}^0 are electronegativity and atomic hardness, respectively. J_{AB} is a function that describes pairwise interaction between two atoms. These individual atomic parameters and pairwise interaction functions are obtained from ReaxFF. The partial derivative of the energy with respect to charge is defined as $\chi_A = \chi_A^0 + J_{AA}^0 Q_A + \sum_{B \neq A} J_{AB} Q_B$. Minimum energy is obtained if $\chi_1 = \chi_2 = \ldots = \chi_N$. Adding the condition on the total charge, $Q_{tot} = \sum_{A=1}^{N} Q_A$ gives a system of N equations solving which, partial atomic charges can be obtained. Therefore, in every time step of MD simulations, the atomic charges are calculated self-consistently. To describe switching at voltage $\pm V$, the electronegativity of Ni atoms in the lower electrode is changed to $\chi^0 \rightarrow \chi^0 \mp V$, where χ^0 is the electronegativity value of Ni atom obtained from ReaxFF parameters.

DFT calculations are performed using Vienna *Ab intio* Simulation Package (VASP)[47,48] with projected augmented wave method (PAW) and GGA-PBE[49] exchange correlation functional. All the calculations are spin-polarized. Grimme DFT-D3 van der Waals correction[50,51] and dipole correction in the z-direction are employed. Gaussian smearing method with a smearing width of 0.05 eV is used. The energy cutoff is set to 520 V. For geometry optimization, 30/a × 30/b × 1 k-points grids are used, where a and b are the lengths of the lattice parameters in the in-plane direction. The energy error is set to 10^{-5} eV in the self-convergent cycle. During geometry optimization, the maximum force on every atom is set to 0.05 eV/Å. For Bader charge[52,53] and ELF calculations, 60/a × 60/b × 1 k-points are used. DDEC bond analysis for the electrode atoms is performed using Lobster tool.[54,55]

Quantum transport calculation is performed using DFT- non-equilibrium Green's function (NEGF)[56] method implemented in the QuantumATK[57] transport calculation module. Spin-polarized DFT calculations are done using LCAO (linear combination of atomic orbital) basis set with "medium" accuracy and SG15 norm-conserving pseudopotentials.[58,59] Surface area of the device is 8.63×9.97 Å^2. An energy cutoff of 105 Ha and a Monkhorst–Pack k-point grid of $3 \times 3 \times 155$ are used. Grimme DFT-D3 van der Waal correction is also employed. For solving Poisson equations, periodic boundary conditions are used in the in-plane (x–y) directions, while Dirichlet boundary condition is applied in the transport direction (z).

III. RESULTS AND DISCUSSIONS

A. Movement of h-BN layer and peeling of Ni atoms

The schematic of the device structure is shown in Fig. 1. Four layers of ⟨111⟩ cleaved surfaces of Ni are added on the top and bottom of monolayer h-BN. During the MD simulations, the outer two Ni layers on both sides are fixed to emulate the behavior of bulk electrodes. The interatomic interactions have been described using ReaxFF[60] that can accurately describe chemical reactions with

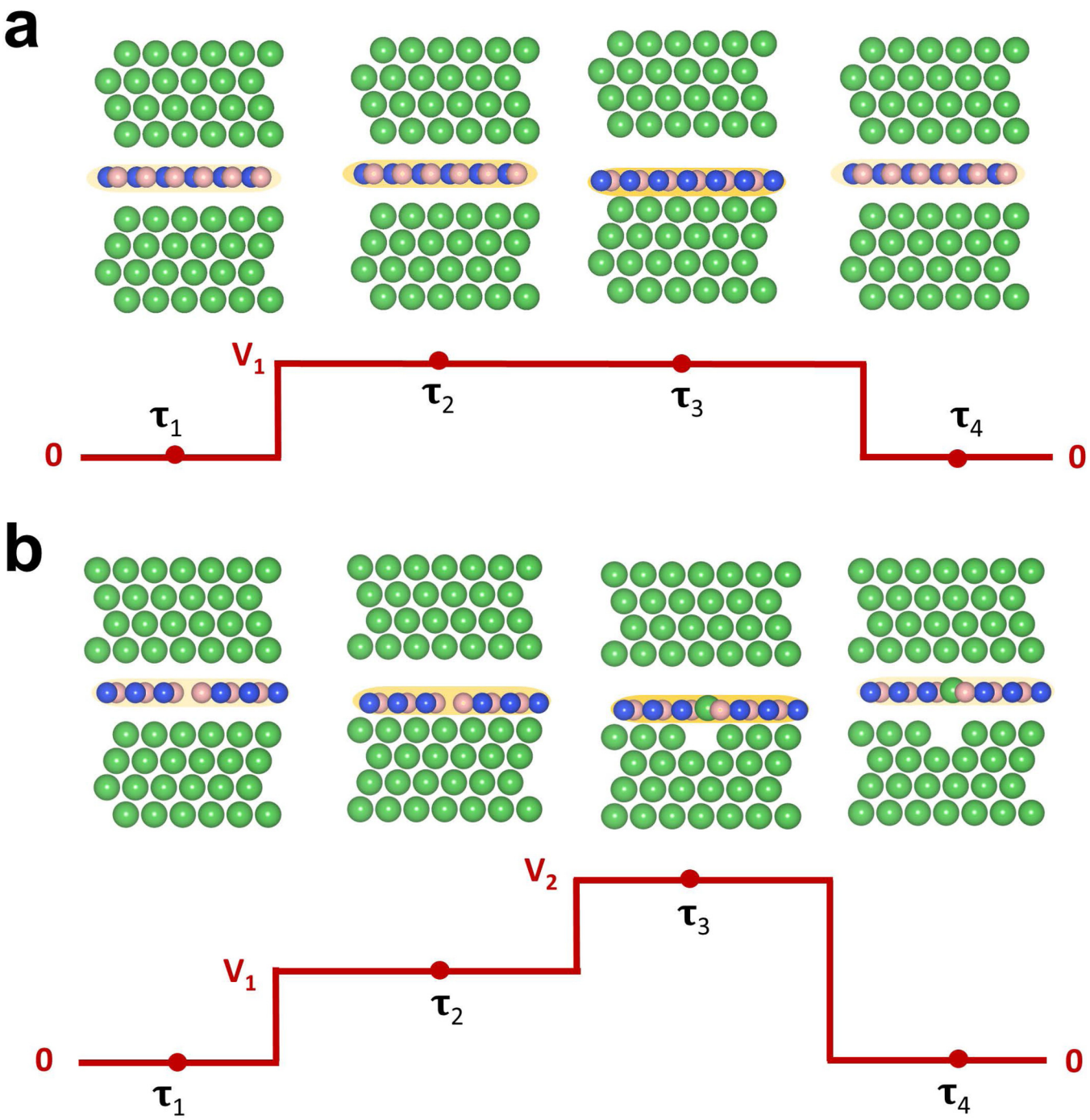

FIG. 1. Details of switching mechanism. (a) Schematics of voltage application in the bottom electrode of Ni/ML h-BN/Ni structure with no vacancy in h-BN. It shows at a certain bias V_1 after time τ_3 due to large negative charge built-up h-BN shifts toward the bottom electrode. As the bias is withdrawn, the h-BN film returns to its original location. (b) Schematics of voltage application in Ni/h-BN/Ni consisting of one N vacancy. As the bias is increased to V_1, the h-BN film shifts toward the bottom electrode. No movement of Ni atom is found. As the bias is further increased to V_2, one Ni atom from the bottom electrode moves into the vacancy center. As the bias is withdrawn, the h-BN film returns to its initial location; however, Ni atom remains inside the vacancy center. B, N, and Ni atoms are represented by pink, blue, and green balls, respectively. The background yellow color of the h-BN layer represents a net negative charge in h-BN. The more intense the color is, the more is the net negative charge.

a much lower computational cost compared to *ab initio* simulations. ReaxFF has been successfully used to describe metallic filament formation[12] and oxygen vacancy migration[61] in bulk oxide-based resistive switching devices. The atomic charges are computed on-the-fly during the MD simulation using the QEq method.[46] The external potential difference between the two electrodes can be accomplished by varying the electronegativity of the electrode atoms according to the applied voltage.[12,62,63] To evaluate the switching mechanism, we consider that the top electrode is grounded and a voltage V is applied at the bottom electrode as described in Section Calculation Details. With the QEq method, the atomic charges are adjusted in accordance with the atomic configurations and the applied bias in every time step of MD simulations.

In Fig. 1(a), the schematics of voltage application in pristine h-BN based devices are depicted. We found that after a certain voltage, the h-BN layer moves toward the lower Ni electrode. In h-BN, due to the electronegativity difference between B and N atoms, the electrons tend to localize around the N atoms. We have found the same from the first-principle-based electron-localization-function (ELF) calculation of pristine h-BN [Fig. S1(a) in the supplementary material]. The polarity of the B–N bond causes partial charges around the atomic centers. We have evaluated the charge distribution in the h-BN layer at different stages of MD simulations. In pristine h-BN without the Ni electrode, B and N contribute an opposite and equal amount of charge, resulting in zero net charge in the h-BN layer. The values obtained from ReaxFF/QEq method are +0.54 and −0.54 e for B and N, respectively. Once Ni electrodes are added, minor charge transfer takes place between Ni and h-BN layer, causing charge redistribution in h-BN. Due to localized electrons, N atoms tend to attract more electrons. As a result, N becomes more negatively charged compared to B atoms. At zero bias, the average charges in B and N are +0.47 and −0.51 e, respectively. To verify the ReaxFF computed charges, we have performed Bader charge analysis from plane wave density-functional-theory (DFT) calculations. Bader charges in B and N in the pristine h-BN layer are +2.16 and −2.16 e, respectively, which results in zero net charge. However, like the ReaxFF/QEq method, negative charges in N atoms (−2.19 e) become higher than the positive charges in B atoms (+2.17 e) after adding Ni layers. Furthermore, we have computed ReaxFF charges for different vacancies in the h-BN film and compared the same with Bader charges (Table S1 in the supplementary material). Although the values of the individual atomic charges in ReaxFF are underestimated compared to Bader charges, the negative charge accumulation around N atomic centers and charge redistribution due to the formation of vacancies can accurately be predicted from ReaxFF/QEq method.

Application of voltage leads to the redistribution of charge in the h-BN layer. When a positive bias is applied at the bottom electrode, the surface Ni atoms become positively charged, and electrons are transferred to the h-BN layer. Due to higher electronegativity, N atoms try to accumulate more electrons, increasing the net negative charge in the h-BN layer. As the bias increases, due to the significant rise in opposite charges, a strong Coulombic attraction force acts between the h-BN and Ni layer resulting in movement of the h-BN toward the electrode [Fig. 1(a)]. The ground state interlayer distance between Ni and h-BN is about 3.2 Å. After shifting, the distance is reduced to around 2.2 Å. In a pristine h-BN based device with a surface area of $4.4 \times 4.7\ nm^2$, the shifting is observed at a positive bias of 4 V after a 59 ps MD run. We have calculated the charges at different time frames: at 25 ps, before the movement, the net charge in h-BN is about −39.9 e, and the surface Ni layer is about +42.5 e. At 59 ps, during the time of movement, the net charge in h-BN and Ni increases to −56.0 and +69.1 e, respectively. As soon as the bias is withdrawn, h-BN restores its original charge state and moves to its initial location (video 1 in the supplementary material). Therefore, the movement of the h-BN layer is a voltage-induced metastable phenomenon entirely due to charge build-up and consequent Coulombic interaction. Also, from DFT calculations, we found that the ELF of h-BN is not spherical but ellipsoidal [Fig. S1(a) in the supplementary material], with the major axis along the vertical z-direction implying a finite dipole moment toward the vertical axis. Due to the dipole moment, on application of the external bias, the h-BN atoms are expected to get attracted toward the oppositely charged metal atoms.

We next add vacancies in h-BN and evaluate the effect of applied bias on it. Single boron or nitrogen vacancies commonly exist in the h-BN film.[36,64,65] Figure 1(b) shows the schematics of a single nitrogen vacancy-embedded h-BN layer stacked between two Ni electrodes. Similar to pristine h-BN, after a certain positive bias, the h-BN layer shifts toward the bottom electrode. As the bias is further increased, at a critical value, the Ni ion from the bottom electrode moves into the vacancy location. The occupation of the Ni atom into the vacancy leads to the formation of conductive nano filament in the device, suggesting switching from HRS to LRS. As the positive bias is withdrawn, the h-BN film returns to its initial location, but the Ni atom remains inside the vacancy center, implying a nonvolatile operation.

The peeling process involves chemical interactions between Ni and vacancy neighboring B atoms. The movement of the h-BN layer is responsible for such chemical reactions. At equilibrium, the Ni electrode and the h-BN layer are separated by about 3.2 Å, close to the van der Waals distance. At this distance, there is no chemical interaction between Ni and vacancy surrounding B atoms. As soon as the distance between Ni and h-BN reduces due to the movement of the h-BN layer, the Ni atom situated just below the vacancy starts interacting with the three B atoms surrounding the vacancy. The dynamical evolution of partial atomic charges during the peeling process is depicted in Fig. 2. At 0 V, the metal atoms are almost charge neutral, N atoms possess a negative charge of about −0.48 e, B atoms about +0.45 e, and the charge of the B atoms around vacancy centers is about +0.34 e. As a positive bias is applied, the surface Ni atoms become positively charged. After the movement of the h-BN layer, the vacancy nearest Ni atom starts transferring electrons to the vacancy surrounding B atoms. As the bias is sequentially increased, the Ni atom becomes more electropositive by losing electrons while the B atoms become more electronegative by gaining electrons (Fig. 2). Due to the chemical interactions, the Ni atom gradually detaches from the electrode and moves toward the h-BN layer. At a critical bias, the Ni ion finally moves into the vacancy center and creates bonds with the neighboring B atoms. After adsorption into the vacancy center, the Ni

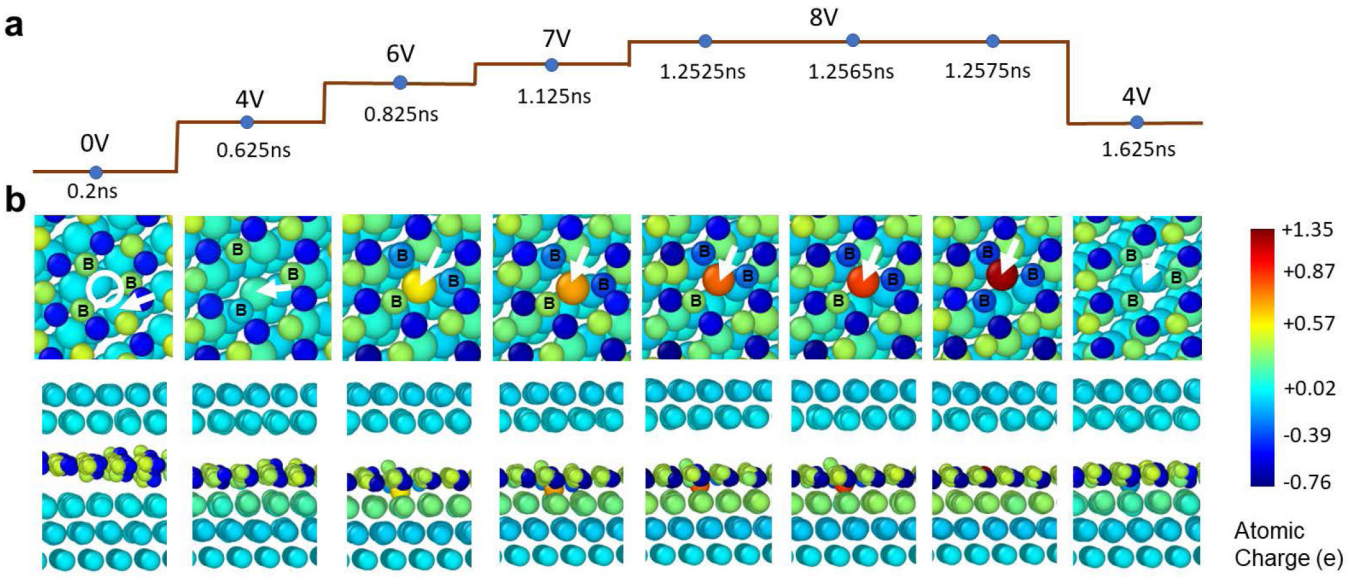

FIG. 2. Charge redistributions in h-BN and Ni during the peeling process. (a) Applied voltages and simulation time frames at which atomistic snapshots are taken. (b) Snapshots showing partial atomic charges. The top and bottom panels show the zoomed-in top-view and side-view images of Ni/h-BN/Ni near N vacancy. The top and bottom electrodes contain four Ni layers each. All electrode layers are not depicted for the clarity of the snapshots. The atoms are colored according to their charge calculated during MD simulations. The color bar shows the values of charge corresponding to different colors. The vacancy location is marked by the white circle (snapshot 1) and Ni atom below the vacancy is pointed by the white arrow. Neighboring B atoms are indicated by their atomic symbols.

ion restores its initial charge-neutral state. The movement of the h-BN layer is primarily responsible for the chemical reactions between Ni and B atoms that further lead to the peeling off of the Ni atom from the electrode and adsorbing in the vacancy center.

In real experiments, the movement of the entire h-BN layer stacked between two Ni electrodes may seem unphysical. Therefore, to make the h-BN layer unsuspended, we have further performed MD simulations on a sample in which the z coordinates of the boundary B and N atoms are fixed (Fig. S2 in the supplementary material) so that the entire h-BN film cannot move. We found that by applying a suitable bias, the central region of the h-BN layer bends toward the electrode, and Ni ions get absorbed into the N vacancies located in this region. The bending of the h-BN layer does not break chemical bonds between the B and N atoms, and it is completely reversible; as soon as the bias is withdrawn, h-BN retains its initial shape. In experiments, wrinkles can form in the h-BN layer during the deposition process due to the thermal expansion difference between the metal and the 2D layer.[36] Such wrinkles can significantly improve the bending flexibility of the 2D layer.[66,67] Therefore, in real devices, it is highly possible that the entire h-BN layer does not move, but some regions are bent toward the Ni electrode due to external voltage. However, the switching mechanism remains the same. The N vacancies in the h-BN region that come close to the metal surface are only responsible for Ni ion absorption. To replicate the experimental device structure and apply boundary restrictions, we must take a sufficiently large sample that is computationally more expensive. As the switching phenomenon remains the same, we conducted further simulations with smaller samples without incorporating any fixed boundary conditions.

B. Bipolar switching process

To provide a detailed atomistic narrative of the RS mechanism, we performed MD simulations on a device of surface area 4.4 nm × 4.7 nm (Fig. S3 in the supplementary material), varying the voltage sequentially. The h-BN flake possesses ten scattered N monovacancies with a vacancy concentration of $4.8 \times 10^{15}/\text{cm}^2$. After the initial heating for 20 ps, we varied the applied voltage in sequence. At each voltage, the simulation is run for 0.25 ns. As the positive voltage is increased to 4 V, the h-BN layer shifts toward the bottom electrode due to a negative charge build-up. But no movement of Ni atoms is found. As the bias is further increased, Ni ions nearest to the vacancy centers start moving into the h-BN plane. At 7 V, four vacancy centers out of the ten are occupied by Ni ions from the bottom electrode. As the voltage is further increased to 8 V, all ten vacancies are filled with Ni. The positive bias is then reduced to 0 V, taking an intermediate bias of 4 V. All the adsorbed Ni atoms remain in the same locations.

Figure 3(a) shows the variations of applied bias and the number of adsorbed Ni atoms in the h-BN layer with simulation time. As mentioned earlier, the external voltage is accomplished by changing the electronegativities of Ni atoms in the bottom electrode. After the SET process, the adsorbed Ni atoms are assigned the standard electronegativity value. However, the switching voltage in the simulation is much higher than the experimental value (near 1 V).[36] As mentioned earlier, ReaxFF underpredicts the

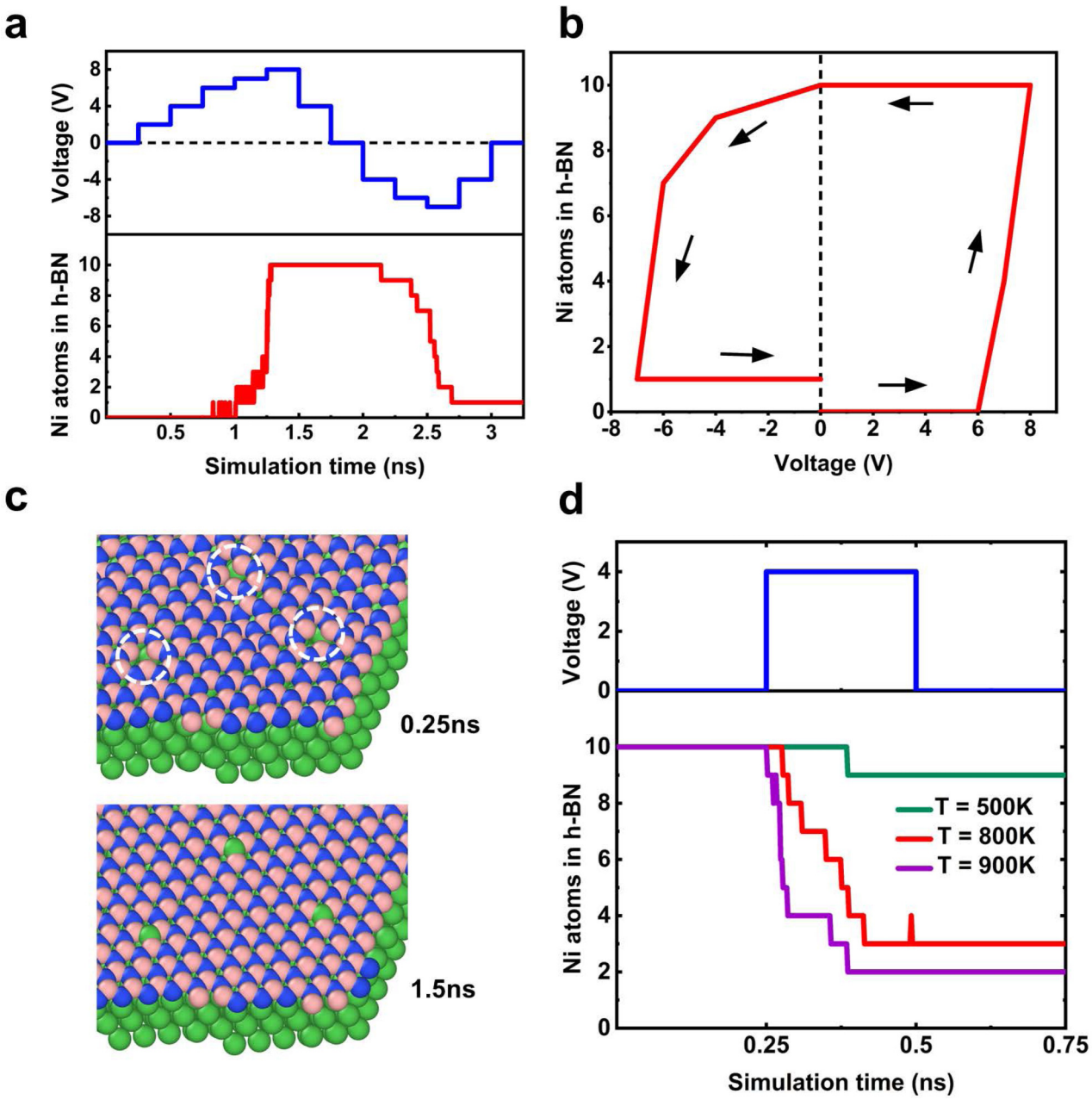

FIG. 3. Bipolar and unipolar switching operation of ML h-BN comprising 10 N vacancies. (a) Plot of applied voltage and number of adsorbed Ni atoms vs simulation time in bipolar switching. (b) Hysteresis plot showing the change in adsorbed Ni atom count with the applied voltage. The order of application of the field is $0 \rightarrow 8 \rightarrow 0 \rightarrow -7 \rightarrow 0$. (c) Atomistic snapshots zooming-in at the vacancy locations at different time frames of MD simulation displaying initial vacancy locations (0.25 ns), Ni atom adsorption after SET (1.5 ns). B, N, and Ni atoms are denoted by pink, blue, and green balls, respectively. The vacancies are marked as white dashed circles. (d) Plot of applied voltage and number of adsorbed Ni atoms at different temperatures vs simulation time in unipolar switching.

individual atomic charges about one-fourth time compared to the Bader charge. Hence, the force exerted on each atom during MD must be much lower than the actual value. Also, the experiment's switching time (~15 ns) is inaccessible in the MD simulations. Therefore, we must raise the bias to visualize switching at a shorter timescale.

During the RESET cycle, the polarity of applied bias is reversed. The return of Ni atoms starts at −4 V. As the bias is

sequentially increased to −7 V, 90% of the adsorbed Ni atoms return to their primary locations. We found that a lower voltage is required to RESET the device compared to SET. The asymmetry in the SET and RESET voltages are also evident in the experimental work.[36] It can be explained from the bond-order analysis of the Ni atoms before and after the SET process. While in the electrode's surface layer, one Ni atom is surrounded by nine neighboring Ni atoms and has a total bond order of about 4.792. After adsorbing in the vacancy location, the Ni atom is bonded with three neighboring B atoms, and the bond order reduces to 3.383. It turns out that a Ni atom in the bulk electrode is more strongly attached to the neighboring atoms than in the vacancy location. As a result, lower bias is required in RESET compared to SET. The hysteresis plot of bipolar switching is shown in Fig. 3(b). In Fig. 3(c), the atomic snapshots near one vacancy location before and after SET are depicted. The videos of SET and RESET cycles are added in videos 2 and 3 in supplementary material.

C. Unipolar switching

In unipolar switching, the RESET voltage should have the same polarity as the SET voltage. Temperature change may play a significant role in this switching. When current flows through nano filament, due to Joule heating, its temperature rises. Recently, measurement of the temperature of the conductive filaments in bulk metal-oxide-based RS devices has been reported.[68] They found that filament temperature can rise to 1300 °C during switching operation. In bulk oxide-based memristors, when the temperature reaches a critical value, the conductive filaments rupture, and the device restores its HRS.[69,70] The rise in temperature in h-BN monolayer-based switches has also been reported.[22]

To understand the unipolar operation, after the SET cycle, we applied a positive RESET voltage of 4 V and raised the device's temperature. At room temperature, there is no movement of Ni atoms. As the device temperature increases, more adsorbed Ni atoms return to their initial locations. In Fig. 3(d), the decrease in the number of Ni atoms in the h-BN film at different temperatures is shown. When the device temperature is raised to 900 K, 80% of the adsorbed Ni atoms return to their primary location. Such a high temperature is assigned to trigger the RESET process within 0.25 ns. RESET can be done at lower temperatures, but the process will be too slow to access in the simulation time frame. We have performed a long run at 600 K and found that 90% of the adsorbed Ni atoms return after 4 ns (Fig. S4 in the supplementary material). In the experiment, the ON current in the unipolar RESET cycle is significantly higher than in the SET cycle. Even the ON current in the bipolar RESET cycle is much lower than in the unipolar RESET. A higher current leads to the rise of filament temperature at a much lower voltage. Therefore, the unipolar switching seems to be dominated by the rise in filament temperature due to Joule heating.

D. Boron vacancy-embedded structure

To determine the role of boron vacancy in RS, we created ten single B vacancies in monolayer h-BN. The device dimension is the same as the N vacancy-embedded device. After initial heating, positive bias pulses of width 0.25 ns are applied in sequence. At 4 V, the shifting of the h-BN layer toward the bottom electrode is observed. However, with increasing bias, no adsorption of Ni atoms inside the vacancy centers is found. To further verify, we manually peeled Ni atoms from the bottom electrode and placed them inside the vacancy centers. MD simulations are then performed at 300 K and zero bias. At the beginning of MD, the peeled Ni atom bonds with the three nearest N atoms and has a total bond order of around 3.80. However, only after a few MD steps, the Ni atoms come out of the h-BN plane and locate between the h-BN and top electrode layer. The snapshots are depicted in Fig. S5 in the supplementary material. Bond analysis shows that the peeled Ni atom creates a bond only with the neighboring 1 N atom near the vacancy and three Ni atoms from the top electrode. The bond order of the Ni atom reduces to around 2.50. However, we repeated the same simulations on N vacancy-embedded structures and found that Ni atoms stay inside the vacancy centers.

Such a difference can be explained by the ELF calculations. The iso-surface plot of ELF for N and B vacancy-embedded h-BN are shown in Figs. S1(b) and S1(c) in the supplementary material, respectively. In pristine h-BN, electrons are more localized around N atoms. When an N vacancy is created, those electrons completely delocalize around the vacancies and spread along the z-direction. Due to this highly delocalized region, any atom near the vacancy is prone to form chemical bonds with the neighboring B atoms. However, in the case of B vacancy, the electrons are entirely localized around the adjacent N atoms. The electron density at the B vacancy center is absolutely zero. Therefore, Ni ions are not likely to be adsorbed inside the B vacancies and create bonds with the neighboring N atoms.

We further investigate the case when N and B vacancies exist together in an h-BN film. MD simulations are carried out on a device consisting of two N mono vacancies, two B mono vacancies, and two BN vacancies. The snapshots are depicted in Fig. S6 in the supplementary material. We found that Ni ions are adsorbed into the N mono vacancies and N vacancy centers in the BN vacancies. There is no adsorption of Ni ions into the B vacancy centers. Earlier work suggests metal atoms can occupy both B and N vacancies during RS.[36] From MD simulations and DFT study, we may conclude N vacancies are primarily responsible for nano-filament formation in monolayer h-BN based devices.

E. Transport properties

To get insight into the resistivity change before and after the SET process, we evaluate the transport properties of the device based on spin-polarized DFT-NEGF formalism. For transport calculation, h-BN is vertically interfaced with 8 Ni layers on both sides. The outer three layers on each side are considered electrode regions, while the inner five layers along with the h-BN layer are set as the central scattering region. The number of Ni layers is increased to make the central scattering region sufficiently large compared to the electrode region. If the central region is short, spurious scattering may occur at the electrode interfaces resulting in poor convergence and inaccurate results. With the same electrode configuration, we have done the MD simulation and found that the

change in the number of Ni layers does not affect any movement of atoms. The SET and RESET voltages remain the same.

The device configurations in transport calculations are shown in Fig. 4(a). The surface area of the device is around 8.86×9.97 Å^2. One N vacancy is created in the h-BN layer, referred to as OFF state configuration. For ON state configuration, a Ni atom from the bottom electrode is manually placed inside the vacancy location. Figure 4(b) illustrates the local device density of states (LDDOS) at the Fermi level for OFF and ON state configurations around the YZ plane. Spin up and spin down densities are summed up. It is clearly visible that the vacancy region becomes more conductive after adsorbing Ni, leading to the formation of conductive nano filament and an increase of overall electron density in the central scattering region. As a result, more current flows through the device.

The zero-bias transmission spectra in the energy range −0.1 to +0.1 V are shown in Fig. 4(c). It is found that the ON state transmission is sufficiently high compared to the OFF state. For the OFF state, the up-spin and down-spin transmission at the Fermi level are 0.20 and 0.25, respectively. However, the transmission values increase to 1.31 and 1.81, respectively, in the ON state. The electrical conductance at room temperature has been evaluated using the following expression:

$$G(E) = \frac{2q^2}{h}\int_{-\infty}^{+\infty}\tau(E)\left(-\frac{\partial f(E, E_F, T)}{\partial E}\right)dE,$$

where $\tau(E)$ is the sum of spin up and spin down transmission coefficients and $f(E, E_F, T)$ is the Fermi–Dirac distribution function with E_F being the Fermi-energy.

The computed conductance values for the OFF state and ON state are 1.62×10^{-5} and 11.99×10^{-5} S, respectively. Hence, about a 7.4 times increase of zero-bias conductance after Ni adsorption is observed. In experiments, the conductivities are usually measured in finite bias. Therefore, comparing the quantitative change in conductivity with the experiments is difficult. The finite bias calculations are not included in this work as they are more expensive, and SCF convergence is extremely difficult. However, the zero-bias calculation identifies two distinct resistance states before and after Ni adsorption.

F. Endurance study

One of the major concerns of these atomically thin devices is that their endurance is usually limited to <100 dc cycles, much lower than amorphous oxide-based devices.[71] In h-BN based thinnest memristive device, an endurance of 50 DC cycles was reported. One of the possible causes behind the irreversibility of the cyclic operation is a rise in device temperature. After several operational cycles, due to Joule heating, the device temperature may increase significantly.[22] To determine the heating effect, we repeated the MD simulation for the bipolar switching cycle at a higher temperature of about 800 K (Fig. S7 in the supplementary material). As the SET voltage is applied, due to the high temperature, several Ni ions from the bottom electrode migrate through a single N vacancy toward the other side of the h-BN film. These ions cannot be retrieved back to their initial locations by applying RESET voltage,

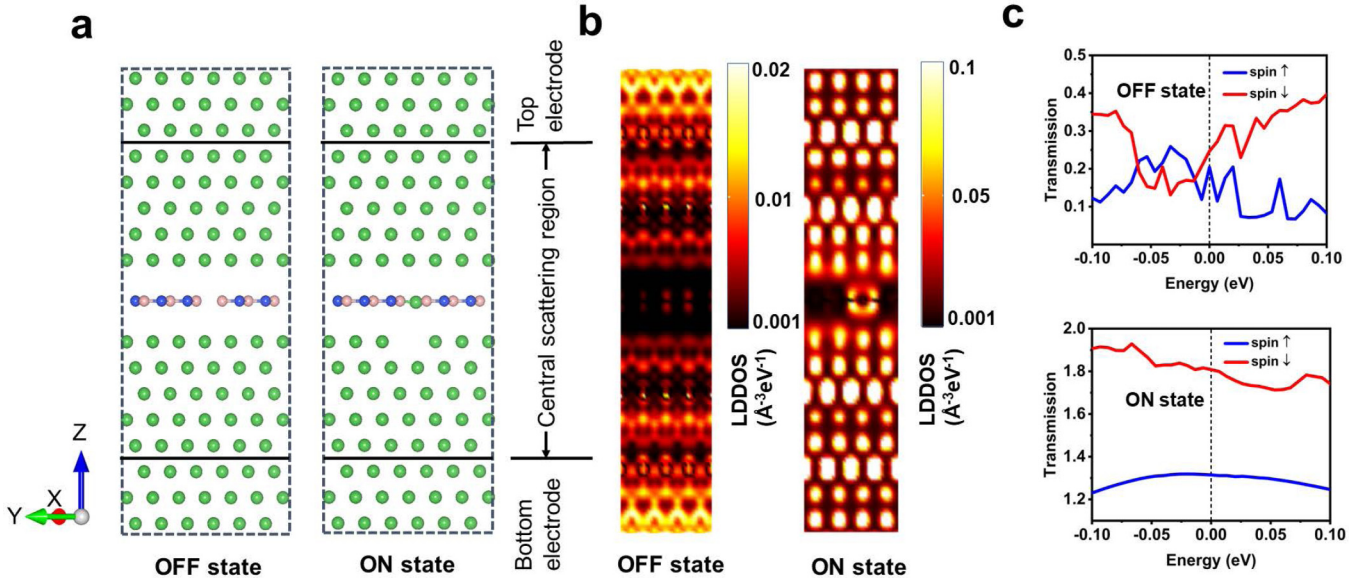

FIG. 4. Quantum transport calculation before and after Ni adsorption. (a) Schematic of Ni/h-BN/Ni device used for transmission calculations. The left image shows h-BN film with one N vacancy, designated as OFF STATE configuration, and the right side image shows Ni atom from the bottom electrode placed in the vacancy center, designated as ON STATE configuration. (b) Plot of local device density of states (LDDOS) along the YZ plane for OFF and ON states. (c) Plot of transmission with respect to energy near the Fermi level for both OFF STATE and ON STATE.

resulting in a breakdown of the reversible switching cycle. Filament formation and rupture are much simpler in amorphous materials due to substantial interstitial spaces throughout the amorphous layer. However, in crystalline 2D materials, the possible space for metal ion migration is through vacancies and grain boundaries. So, if the metal ions migrate uncontrollably through these atomic scale regions and reach the other side of h-BN, returning them to their initial locations is not easy. Only the ions absorbed in the vacancy centers can be adequately restored. So, uncontrollable movements of metal ions may lead to irreversible switching. In a recent work, a polymer layer was inserted between h-BN and top electrodes to prevent the overgrowth of filaments.[72] That device showed a better endurance of 100 DC cycles compared to a pure h-BN based device. From MD simulations, it is evident that temperature rise can trigger such uncontrolled penetration of metal ions through defects that cannot be restored during the reverse cycle.

IV. CONCLUSIONS

For the first time, we present a detailed picture of "nanofilament" formation in ML h-BN during the nonvolatile RS operation. Metal ion adsorption and desorption in the N vacancy centers are primarily responsible for resistive switching. This simulation can accurately describe forming free bipolar and unipolar switching phenomena. It provides a detailed understanding of the role of individual vacancies in the switching process. We have also looked into the cause of the lower endurance of such devices. At room temperature, the process of metal atom adsorption is highly reversible. However, with temperature rise, unrestricted migration of metal ions may lead to the breakdown of the switching cycle. So, a good heat sink is needed to increase the endurance of such devices. Although we have only investigated explicit Ni electrodes (DDEC bond order 2.49), the proposed mechanism can also be applicable to other active electrodes like Au (DDEC bond order 2.88). The dynamic evaluation of switching is performed using the reactive force field, whose parameters are absolutely not application-specific and entirely trained from fundamental physical and chemical data. Hence, this simulation may be useful to design reliable and high-performance memristive devices by exploring new materials and designs.

SUPPLEMENTARY MATERIAL

See the supplementary material for details of electron-localization-function, MD run with fixed boundary atoms, device configuration in atomic scale, long time scale unipolar RESET, MD simulations of Ni atoms inside B vacancy, Ni adsorption on BN vacancy, high temperature MD simulations, and calculated atomic charges.

ACKNOWLEDGMENTS

This work was supported by the National Supercomputing Mission (NSM) Project Framework under Grant No. DST/NSM/R&D_HPC_Applications/2021/33. The authors acknowledge the Supercomputer Education and Research Center (SERC), Indian Institute of Science (IISc) Bangalore, and the Center For Development Of Advanced Computing (CDAC), Pune for CPU- and GPU-based computations.

AUTHOR DECLARATIONS

Conflict of Interest

The authors have no conflicts to disclose.

Author Contributions

S. Mitra performed the MD simulations and the DFT calculations and analyzed the results. S. Mahapatra conceived the problem statement and overall supervised the work. All authors contributed to the writing.

Sanchali Mitra: Data curation (lead); Formal analysis (lead); Investigation (lead); Methodology (lead); Validation (lead); Writing – original draft (lead). **Santanu Mahapatra:** Conceptualization (lead); Funding acquisition (lead); Supervision (lead); Writing – review & editing (lead).

DATA AVAILABILITY

Main data supporting the findings of this study are available within the article and its supplementary material. Other relevant data are available from the corresponding author upon reasonable request.

REFERENCES

[1]L. Mario, S. Abu, L. W. D, L. G. Manuel, C. Meng-Fan, A. Deji, F. M. Puglisi, H. N. Alshareef, L. Ming, and J. B. Roldan, "Memristive technologies for data storage, computation, encryption, and radio-frequency communication," Science **376**(6597), eabj9979 (2022).
[2]T. Shi, R. Wang, Z. Wu, Y. Sun, J. An, and Q. Liu, "A review of resistive switching devices: Performance improvement, characterization, and applications," Small Struct. **2**(4), 2000109 (2021).
[3]F. Zahoor, T. Z. Azni Zulkifli, and F. A. Khanday, "Resistive random access memory (RRAM): An overview of materials, switching mechanism, performance, multilevel cell (Mlc) storage, modeling, and applications," Nanoscale Res. Lett. **15**(1), 90 (2020).
[4]S. Slesazeck and T. Mikolajick, "Nanoscale resistive switching memory devices: A review," Nanotechnology **30**(35), 352003 (2019).
[5]L. Chua, "Memristor–The missing circuit element," IEEE Trans. Circuit Theory **18**(5), 507–519 (1971).
[6]D. B. Strukov, G. S. Snider, D. R. Stewart, and R. S. Williams, "The missing memristor found," Nature **453**(7191), 80–83 (2008).
[7]R. Khan, N. Ilyas, M. Z. M. Shamim, M. I. Khan, M. Sohail, N. Rahman, A. A. Khan, S. N. Khan, and A. Khan, "Oxide-based resistive switching-based devices: Fabrication, influence parameters and applications," J. Mater. Chem. C **9**, 15755–15788 (2021).
[8]B. Mohammad, M. A. Jaoude, V. Kumar, D. M. al Homouz, H. A. Nahla, M. Al-Qutayri, and N. Christoforou, "State of the art of metal oxide memristor devices," Nanotechnol. Rev. **5**(3), 311–329 (2016).
[9]W. Sun, B. Gao, M. Chi, Q. Xia, J. J. Yang, H. Qian, and H. Wu, "Understanding memristive switching via *in situ* characterization and device modeling," Nat. Commun. **10**, 3453 (2019).
[10]Y. Yang, P. Gao, L. Li, X. Pan, S. Tappertzhofen, S. Choi, R. Waser, I. Valov, and W. D. Lu, "Electrochemical dynamics of nanoscale metallic inclusions in dielectrics," Nat. Commun. **5**, 4232 (2014).

[11]Z. Wang, M. Rao, R. Midya, S. Joshi, H. Jiang, P. Lin, W. Song, S. Asapu, Y. Zhuo, C. Li, H. Wu, Q. Xia, and J. J. Yang, "Threshold switching of Ag or Cu in dielectrics: Materials, mechanism, and applications," Adv. Funct. Mater. **28**(6), 1704862 (2018).
[12]N. Onofrio, D. Guzman, and A. Strachan, "Atomic origin of ultrafast resistance switching in nanoscale electrometallization cells," Nat. Mater. **14**(4), 440–446 (2015).
[13]C. Li, B. Gao, Y. Yao, X. Guan, X. Shen, Y. Wang, P. Huang, L. Liu, X. Liu, J. Li, C. Gu, J. Kang, and R. Yu, "Direct observations of nanofilament evolution in switching processes in HfO_2-based resistive random access memory by *in situ* TEM studies," Adv. Mater. **29**(10), 1602976 (2017).
[14]Y. Yang, X. Zhang, L. Qin, Q. Zeng, X. Qiu, and R. Huang, "Probing nanoscale oxygen ion motion in memristive systems," Nat. Commun. **8**, 15173 (2017).
[15]R. Ge, X. Wu, L. Liang, S. M. Hus, Y. Gu, E. Okogbue, H. Chou, J. Shi, Y. Zhang, S. K. Banerjee, Y. Jung, J. C. Lee, and D. Akinwande, "A library of atomically thin 2D materials featuring the conductive-point resistive switching phenomenon," Adv. Mater. **33**(7), 2007792 (2021).
[16]L. Wang, X. Shen, Z. Gao, J. Fu, S. Yao, L. Cheng, and X. Lian, "Review of applications of 2D materials in memristive neuromorphic circuits," J. Mater. Sci. **57**, 4915–4940 (2022).
[17]K. Tang, Y. Wang, C. Gong, C. Yin, M. Zhang, X. Wang, and J. Xiong, "Electronic and photoelectronic memristors based on 2D materials," Adv. Electron. Mater. **8**, 2101099 (2022).
[18]G. Cao, P. Meng, J. Chen, H. Liu, R. Bian, C. Zhu, F. Liu, and Z. Liu, "2D material based synaptic devices for neuromorphic computing," Adv. Funct. Mater. **31**(4), 2005443 (2021).
[19]K. C. Kwon, J. H. Baek, K. Hong, S. Y. Kim, and H. W. Jang, "Memristive devices based on two-dimensional transition metal chalcogenides for neuromorphic computing," Nanomicro Lett. **14**(1), 58 (2022). .
[20]C. Wen, X. Li, T. Zanotti, F. M. Puglisi, Y. Shi, F. Saiz, A. Antidormi, S. Roche, W. Zheng, X. Liang, J. Hu, S. Duhm, J. B. Roldan, T. Wu, V. Chen, E. Pop, B. Garrido, K. Zhu, F. Hui, and M. Lanza, "Advanced data encryption using 2D materials," Adv. Mater. **33**(27), 2100185 (2021).
[21]M. Kim, R. Ge, X. Wu, X. Lan, J. Tice, J. C. Lee, and D. Akinwande, "Zero-static power radio-frequency switches based on MoS_2 atomristors," Nat. Commun. **9**(1), 2524 (2018).
[22]M. Kim, E. Pallecchi, R. Ge, X. Wu, G. Ducournau, J. C. Lee, H. Happy, and D. Akinwande, "Analogue switches made from boron nitride monolayers for application in 5G and terahertz communication systems," Nat. Electron. **3**, 479–485 (2020).
[23]S. Chen, Z. Lou, D. Chen, and G. Shen, "An artificial flexible visual memory system based on an UV-motivated memristor," Adv. Mater. **30**(7), 1705400 (2018).
[24]X. Feng, X. Liu, and K.-W. Ang, "2D photonic memristor beyond graphene: Progress and prospects," Nanophotonics **9**(7), 1579–1599 (2020).
[25]S. Roy, X. Zhang, A. B. Puthirath, A. Meiyazhagan, S. Bhattacharyya, M. M. Rahman, G. Babu, S. Susarla, S. K. Saju, M. K. Tran, L. M. Sassi, M. A. S. R. Saadi, J. Lai, O. Sahin, S. M. Sajadi, B. Dharmarajan, D. Salpekar, N. Chakingal, A. Baburaj, X. Shuai, A. Adumbumkulath, K. A. Miller, J. M. Gayle, A. Ajnsztajn, T. Prasankumar, V. V. J. Harikrishnan, V. Ojha, H. Kannan, A. Z. Khater, Z. Zhu, S. A. Iyengar, P. A. S. Autreto, E. F. Oliveira, G. Gao, A. G. Birdwell, M. R. Neupane, T. G. Ivanov, J. Taha-Tijerina, R. M. Yadav, S. Arepalli, R. Vajtai, and P. M. Ajayan, "Structure, properties and applications of two-dimensional hexagonal boron nitride," Adv. Mater. **33**(44), 2101589 (2021). https://doi.org/10.1002/adma.202101589
[26]D. Wickramaratne, L. Weston, and C. G. van de Walle, "Monolayer to bulk properties of hexagonal boron nitride," J. Phys. Chem. C **122**(44), 25524–25529 (2018).
[27]K. Zhang, Y. Feng, F. Wang, Z. Yang, and J. Wang, "Two dimensional hexagonal boron nitride (2D-HBN): Synthesis, properties and applications," J. Mater. Chem. C Mater. **5**(46), 11992–12022 (2017).
[28]C. Pan, Y. Ji, N. Xiao, F. Hui, K. Tang, Y. Guo, X. Xie, F. M. Puglisi, L. Larcher, E. Miranda, L. Jiang, Y. Shi, I. Valov, P. C. McIntyre, R. Waser, and M. Lanza, "Coexistence of grain-boundaries-assisted bipolar and threshold resistive switching in multilayer hexagonal boron nitride," Adv. Funct. Mater. **27**(10), 1604811 (2017).
[29]Y. Shi, X. Liang, B. Yuan, V. Chen, H. Li, F. Hui, Z. Yu, F. Yuan, E. Pop, H.-S. P. Wong, and M. Lanza, "Electronic synapses made of layered two-dimensional materials," Nat. Electron. **1**(8), 458–465 (2018).
[30]P. Zhuang, W. Lin, J. Ahn, M. Catalano, H. Chou, A. Roy, M. Quevedo-Lopez, L. Colombo, W. Cai, and S. K. Banerjee, "Nonpolar resistive switching of multilayer-HBN-based memories," Adv. Electron. Mater. **6**(1), 1900979 (2020).
[31]S. Chen, M. R. Mahmoodi, Y. Shi, C. Mahata, B. Yuan, X. Liang, C. Wen, F. Hui, D. Akinwande, D. B. Strukov, and M. Lanza, "Wafer-scale integration of two-dimensional materials in high-density memristive crossbar arrays for artificial neural networks," Nat. Electron. **3**(10), 638–645 (2020).
[32]B. Yuan, X. Liang, L. Zhong, Y. Shi, F. Palumbo, S. Chen, F. Hui, X. Jing, M. A. Villena, L. Jiang, and M. Lanza, "150 nm × 200 nm cross-point hexagonal boron nitride-based memristors," Adv. Electron. Mater. **6**(12), 1900115 (2020).
[33]C. Pan, E. Miranda, M. A. Villena, N. Xiao, X. Jing, X. Xie, T. Wu, F. Hui, Y. Shi, and M. Lanza, "Model for multi-filamentary conduction in graphene/hexagonalboron-nitride/graphene based resistive switching devices," 2D Mater. **4**(2), 025099 (2017).
[34]D. Zhang, C.-H. Yeh, W. Cao, and K. Banerjee, "0.5T0.5R—An ultracompact RRAM cell uniquely enabled by van Der Waals heterostructures," IEEE Trans. Electron Devices **68**(4), 2033–2040 (2021).
[35]L. Sun, G. Hwang, W. Choi, G. Han, Y. Zhang, J. Jiang, S. Zheng, K. Watanabe, T. Taniguchi, M. Zhao, R. Zhao, Y.-M. Kim, and H. Yang, "Ultralow switching voltage slope based on two-dimensional materials for integrated memory and neuromorphic applications," Nano Energy **69**, 104472 (2020).
[36]X. Wu, R. Ge, P.-A. Chen, H. Chou, Z. Zhang, Y. Zhang, S. Banerjee, M.-H. Chiang, J. C. Lee, and D. Akinwande, "Thinnest nonvolatile memory based on monolayer H-BN," Adv. Mater. **31**(15), 1806790 (2019).
[37]S. Mitra, A. Kabiraj, and S. Mahapatra, "Theory of nonvolatile resistive switching in monolayer molybdenum disulfide with passive electrodes," npj 2D Mater. Appl. **5**(1), 33 (2021).
[38]S. Plimpton, "Fast parallel algorithms for short-range molecular dynamics," J. Comput. Phys. **117**(1), 1–19 (1995).
[39]H. Carter Edwards, C. R. Trott, and D. Sunderland, "Kokkos: Enabling many-core performance portability through polymorphic memory access patterns," J. Parallel Distrib. Comput. **74**(12), 3202–3216 (2014).
[40]K. Momma and F. Izumi, "*VESTA 3* for three-dimensional visualization of crystal, volumetric and morphology data," J. Appl. Crystallogr. **44**(6), 1272–1276 (2011).
[41]A. Stukowski, "Visualization and analysis of atomistic simulation data with OVITO—The open visualization tool," Model. Simul. Mater. Sci. Eng. **18**(1), 015012 (2009).
[42]S. S. Han, J. K. Kang, H. M. Lee, A. C. T. van Duin, and W. A. Goddard, "The theoretical study on interaction of hydrogen with single-walled boron nitride nanotubes. I. The reactive force field $ReaxFF_{HBN}$ development," J. Chem. Phys. **123**(11), 114703 (2005).
[43]J. E. Mueller, A. C. T. van Duin, and W. A. Goddard, "Development and validation of ReaxFF reactive force field for hydrocarbon chemistry catalyzed by nickel," J. Phys. Chem. C **114**(11), 4939–4949 (2010).
[44]S. Liu, A. C. T. van Duin, D. M. van Duin, B. Liu, and J. H. Edgar, "Atomistic insights into nucleation and formation of hexagonal boron nitride on nickel from first-principles-based reactive molecular dynamics simulations," ACS Nano **11**(4), 3585–3596 (2017).
[45]D. Stradi, L. Jelver, S. Smidstrup, and K. Stokbro, "Method for determining optimal supercell representation of interfaces," J. Phys.: Condens. Matter **29**(18), 185901 (2017).
[46]A. K. Rappe and W. A. Goddard, "Charge equilibration for molecular dynamics simulations," J. Phys. Chem. **95**(8), 3358–3363 (1991).
[47]G. Kresse and D. Joubert, "From ultrasoft pseudopotentials to the projector augmented-wave method," Phys. Rev. B **59**(3), 1758–1775 (1999).
[48]G. Kresse and J. Furthmüller, "Efficient iterative schemes for *ab initio* total-energy calculations using a plane-wave basis set," Phys. Rev. B **54**(16), 11169–11186 (1996).

[49]J. P. Perdew, K. Burke, and M. Ernzerhof, "Generalized gradient approximation made simple," Phys. Rev. Lett. **77**(18), 3865–3868 (1996).
[50]J. Moellmann and S. Grimme, "DFT-D3 study of some molecular crystals," J. Phys. Chem. C **118**(14), 7615–7621 (2014).
[51]S. Grimme, S. Ehrlich, and L. Goerigk, "Effect of the damping function in dispersion corrected density functional theory," J. Comput. Chem. **32**(7), 1456–1465 (2011).
[52]M. Yu and D. R. Trinkle, "Accurate and efficient algorithm for Bader charge integration," J. Chem. Phys. **134**(6), 064111 (2011).
[53]E. Sanville, S. D. Kenny, R. Smith, and G. Henkelman, "Improved grid-based algorithm for bader charge allocation," J. Comput. Chem. **28**(5), 899–908 (2007).
[54]S. Maintz, V. L. Deringer, A. L. Tchougréeff, and R. Dronskowski, "LOBSTER: A tool to extract chemical bonding from plane-wave based DFT," J. Comput. Chem. **37**(11), 1030–1035 (2016).
[55]R. Nelson, C. Ertural, J. George, V. L. Deringer, G. Hautier, and R. Dronskowski, "LOBSTER: Local orbital projections, atomic charges, and chemical-bonding analysis from projector-augmented-wave-based density-functional theory," J. Comput. Chem. **41**(21), 1931–1940 (2020).
[56]M. Brandbyge, J.-L. Mozos, P. Ordejón, J. Taylor, and K. Stokbro, "Density-functional method for nonequilibrium electron transport," Phys. Rev. B **65**(16), 165401 (2002).
[57]S. Smidstrup, T. Markussen, P. Vancraeyveld, J. Wellendorff, J. Schneider, T. Gunst, B. Verstichel, D. Stradi, P. A. Khomyakov, U. G. Vej-Hansen, M.-E. Lee, S. T. Chill, F. Rasmussen, G. Penazzi, F. Corsetti, A. Ojanperä, K. Jensen, M. L. N. Palsgaard, U. Martinez, A. Blom, M. Brandbyge, and K. Stokbro, "QuantumATK: An integrated platform of electronic and atomic-scale modelling tools," J. Phys.: Condens. Matter **32**(1), 015901 (2019).
[58]D. R. Hamann, "Optimized norm-conserving Vanderbilt pseudopotentials," Phys. Rev. B **88**(8), 85117 (2013).
[59]M. Schlipf and F. Gygi, "Optimization algorithm for the generation of ONCV pseudopotentials," Comput. Phys. Commun. **196**, 36–44 (2015).
[60]T. P. Senftle, S. Hong, M. M. Islam, S. B. Kylasa, Y. Zheng, Y. K. Shin, C. Junkermeier, R. Engel-Herbert, M. J. Janik, H. M. Aktulga, T. Verstraelen, A. Grama, and A. C. T. van Duin, "The ReaxFF reactive force-field: Development, applications and future directions," npj Comput. Mater. **2**(1), 15011 (2016).
[61]M. L. Urquiza, M. M. Islam, A. C. T. van Duin, X. Cartoixà, and A. Strachan, "Atomistic insights on the full operation cycle of a HfO_2-based resistive random access memory cell from molecular dynamics," ACS Nano **15**(8), 12945–12954 (2021).
[62]C. Merlet, B. Rotenberg, P. A. Madden, P.-L. Taberna, P. Simon, Y. Gogotsi, and M. Salanne, "On the molecular origin of supercapacitance in nanoporous carbon electrodes," Nat. Mater. **11**(4), 306–310 (2012).
[63]J. Chen and T. J. Martínez, "Charge conservation in electronegativity equalization and its implications for the electrostatic properties of fluctuating-charge models," J. Chem. Phys. **131**(4), 044114 (2009).
[64]A. Sajid, J. R. Reimers, and M. J. Ford, "Defect states in hexagonal boron nitride: Assignments of observed properties and prediction of properties relevant to quantum computation," Phys. Rev. B **97**(6), 64101 (2018).
[65]J. Zhang, R. Sun, D. Ruan, M. Zhang, Y. Li, K. Zhang, F. Cheng, Z. Wang, and Z.-M. Wang, "Point defects in two-dimensional hexagonal boron nitride: A perspective," J. Appl. Phys. **128**(10), 100902 (2020).
[66]W. Chen, X. Gui, B. Liang, M. Liu, Z. Lin, Y. Zhu, and Z. Tang, "Controllable fabrication of large-area wrinkled graphene on a solution surface," ACS Appl. Mater. Interfaces **8**(17), 10977–10984 (2016).
[67]W. Chen, X. Gui, L. Yang, H. Zhu, and Z. Tang, "Wrinkling of two-dimensional materials: Methods, properties and applications," Nanoscale Horiz. **4**, 291–320 (2019).
[68]S. Deshmukh, M. Muñoz Rojo, E. Yalon, S. Vaziri, C. Koroglu, R. Islam, R. A. Iglesias, K. Saraswat, and E. Pop, "Direct measurement of nanoscale filamentary hot spots in resistive memory devices," Sci. Adv. **8**(13), eabk1514 (2022).
[69]M. Uenuma, Y. Ishikawa, and Y. Uraoka, "Joule heating effect in nonpolar and bipolar resistive random access memory," Appl. Phys. Lett. **107**(7), 073503 (2015).
[70]X. Zhang, L. Xu, H. Zhang, J. Liu, D. Tan, L. Chen, Z. Ma, and W. Li, "Effect of joule heating on resistive switching characteristic in AlOx cells made by thermal oxidation formation," Nanoscale Res. Lett. **15**(1), 11 (2020).
[71]J. Ge, H. Huang, Z. Ma, W. Chen, X. Cao, H. Fang, J. Yan, Z. Liu, W. Wang, and S. Pan, "A sub-500 MV monolayer hexagonal boron nitride based memory device," Mater. Des. **198**, 109366 (2021).
[72]Z. Ma, J. Ge, W. Chen, X. Cao, S. Diao, Z. Liu, and S. Pan, "Reliable memristor based on ultrathin native silicon oxide," ACS Appl. Mater. Interfaces **14**(18), 21207–21216 (2022).